J. Fluid Mech. (1986), *vol.* 162, *pp.* 237–260
Printed in Great Britain

Experimental study of the influence of wind on Benjamin–Feir sideband instability

By LARRY F. BLIVEN†,
Oceanic Hydrodynamics, Inc., Salisbury, MD 21801

NORDEN E. HUANG
NASA Goddard Space Flight Center, Greenbelt, MD 20771

AND STEVEN R. LONG
NASA Goddard Space Flight Center, Wallops Flight Facility,
Wallops Island, VA 23337

(Received 23 July 1984 and in revised form 16 July 1985)

A laboratory investigation of the influence of wind on the evolution of mechanically generated regular (m.g.r.) waves is reported. Surface elevation measurements were made at four fetches for steep ($0.1 < \overline{ak} < 0.2$, 2 Hz) m.g.r. waves, moderate ($15 < u_* < 25$ cm s^{-1}, 3–6 Hz) wind waves, and combinations of the m.g.r. and wind waves. The m.g.r. wave spectra exhibit Benjamin–Feir sidebands that grow exponentially with fetch and whose growth rate increases as the initial wave steepness increases. As fetch increases for the wind cases, total energy increases and the frequency of the spectral maximum downshifts, but no spectral lines representing Benjamin–Feir sidebands were detected even though the wave steepness and fetch were similar to the m.g.r. waves whose spectra displayed sidebands. As wind speed increased over the m.g.r. waves, sideband magnitude, sideband growth rate and low-frequency perturbation components associated with the instability mechanism were reduced.

1. Introduction

Stability analysis of the nonlinear wave equations provides insight into frequency modulation and directional spreading of wave systems. Although the nonlinear equations are usually solved for free (no energy sources or sinks) waves, free-wave results are sometimes used to explain wind-wave phenomena. The purpose of this laboratory investigation is to examine the influence of wind on the evolution of sideband instabilities. These experiments are designed to explore the appropriateness of applying nonlinear free-wave results to active wind-wave-generation conditions. We briefly review previous theoretical studies and supporting experiments in order to elucidate existing results and provide the motivation for the material reported herein.

Benjamin & Feir (1967) showed that, at constant amplitude and frequency, small-amplitude sinusoidal waves subject to low-frequency perturbations evolve such that sidebands develop around the spectral peak. They predicted a resonance-frequency condition for sideband pairs around the dominant wave frequency as

$$f_l + f_h = 2f_0, \tag{1.1}$$

† Present address: NASA Goddard Space Flight Center, Wallops Flight Facility, Wallops Island, VA 23337.

where f_l and f_h are lower- and higher-sideband frequencies and f_0 is the spectral-peak frequency. The maximum growth rate for sideband pairs occurs at normalized sideband frequency ($\delta f/f_0$) determined by the slope (ak) of the dominant wave as

$$\delta f/f_0 = ak, \tag{1.2}$$

where a and k are respectively the amplitude and wavenumber of the dominant wave. The perturbation frequency δf is defined as

$$\delta f = f_0 - f_l. \tag{1.3}$$

The normalized sideband frequency has been referred to as the modulational frequency because in some cases it is related to the number of waves in a group. Recently, McLean *et al.* (1981) and McLean (1982*a*, *b*) presented theoretical analyses that unified subsequent free-wave stability analysis. Their computations, which are based on the full water-wave equations, reveal two distinct types of instabilities for finite-amplitude, free, gravity waves. These were referred to as type-I and type-II instabilities. From the type-I instability, which is predominantly two-dimensional, the well-known Benjamin–Feir (1967) instability, Phillips' (1960) figure 8 resonant diagram, and Longuet-Higgins' (1978) finite-amplitude results were recovered. The type-II instability is usually three-dimensional and becomes dominant when the wave steepness is sufficiently large. The type II had been predicted by Zakharov (1968) and Hasselmann (1979).

Free-wave experiments support these analytic results for both type-I and -II instabilities. The earliest experiments were conducted by Benjamin & Feir (1967) for type-I instabilities. Data from those experiments showed that, as regular waves propagate, sidebands indeed develop near the spectral peak such that the sideband frequency is related to the initial wave steepness and that the sidebands grow exponentially with fetch. Subsequent laboratory data by Lake *et al.* (1977), however, showed that, when the ratio of the sideband to spectral-peak energy is sufficiently large, the growth rates of the sidebands diverge such that the lower sideband grows faster than the upper sideband until ultimately the spectrum peak downshifts to the frequency of the lower sideband. Lake *et al.* could not model the downshift by analysis of the nonlinear Schrödinger equation because analytic results predict initially symmetric sideband components about the carrier frequency and the initial symmetry is preserved throughout the entire Fermi–Pasta–Ulam recurrence process. They suggested and later Melville (1982) confirmed by laboratory experiments that this divergence in sideband development is associated with wave breaking. Type I are subharmonic instabilities which generally occur for steepness of $0 < ak < 0.38$. Type II are much faster-growing instabilities, which were predicted by Longuet-Higgins (1978*a*, *b*) for the two-dimensional case when $ak > 0.40$. McLean *et al.* (1981) extended Longuet-Higgins' result, showing that there are three-dimensional type-II instabilities continuous with the two-dimensional type II for $ak > 0.40$, but which also exist at lower values of ak. Laboratory data by Su (1982) revealed that the skewed waves which were generated by the three-dimensional bifurcation from a uniform wavetrain occurred most clearly when $0.16 < ak < 0.18$. Su also observed three-dimensional structures of symmetric and skewed wave patterns for $ak > 0.25$.

The excellent agreement between theoretical and experimental results for free waves has prompted some investigators to adopt these results for the wind-wave-generation problem. For example, Lake & Yuen (1978) proposed a wind-wave model which represents the wavefield as a single nonlinear wavetrain having a carrier frequency equal to the dominant frequency of the wave spectrum. The model assumes

that wind supplies energy primarily to the dominant wave and that frequency downshifting is achieved by a type-I instability mechanism. They claim that their model is applicable whenever the wave system consists of a coherent one-dimensional dominant wave with mean wave steepness greater than 0.1, regardless of wind speed or wave age. To support the Benjamin–Feir downshift assumption, they presented data that showed that the modulational frequency of steep wind waves is related to the dominant-wave steepness. Later, Longuet-Higgins (1980) showed that his finite wave-instability model fits the wind-wave modulational data more closely than the Benjamin–Feir relationship.

It should be emphasized that the theoretical results for frequency downshifting upon which Lake & Yuen's (1978) wind-wave model are based were obtained for freely travelling waves without wind forcing. Even though wind-wave time series provide evidence of wave groups, as are observed for free regular waves with sidebands, there is only limited evidence (Hatori 1984) to show that the modulation may be generated by a type-I instability. Theoretical analysis conducted for freely travelling waves assumes no energy sources or sinks, so the results do not provide any information concerning the influence of energy input or output from mechanisms such as wind stress or wave breaking. These mechanisms, however, are certainly important for wave generation and decay. For example, Melville (1982) presented laboratory paddle-generated-wave data showing that the downshift of the carrier wave to the lower sideband in type-I instabilities is associated with wave breaking. Hatori & Toba (1983) investigated the transition of mechanically generated regular waves to wind waves under the action of strong wind ($u_* = 59$ cm s^{-1}) which generated active wave breaking and found that, although the modulation shared some characteristics with Benjamin–Feir-type instabilities, other characteristics revealed that the frequency shift was due to the mutual coalescence of waves as reported by Mollo-Christensen & Ramamonjiarisoa (1982). Moreover, recent theoretical work also casts doubts upon direct application of the type-I instability result to the wind-wave-generation problem. For example, Alber (1978) and Crawford, Saffman & Yuen (1980) in analyses of the evolution of a random field of nonlinear, deep-water, free gravity waves found that the effect of randomness is to reduce the growth rate and the extent of the instability compared to a more narrow-banded regular-wave case. Furthermore, Tsimring (1983) provides a wind-wave-generation analysis that predicts that a new second-order instability emerges as a consequence of wind forcing, which has a significantly shorter timescale than the type-I instability. Thus the influence of wind stress on type I instabilities needs to be clarified in order to document the relevance of this mechanism during wind-wave generation.

We report a series of laboratory experiments designed to investigate the influence of wind on the development of type-I instabilities. Steep regular paddle waves are employed in this study as background conditions because they produce type-I instabilities that can be clearly identified as sidebands in spectra. Winds of increasing strength were imposed onto these background conditions. The laboratory experiments monitored steep-paddle, wind, and combined paddle-plus-wind conditions. Thus the modification of sidebands and the wavefield evolution were quantified by analysis of spectra. This approach provides a systematic method to assess the effect of wind on the type-I instability mechanism and the wind-wave-generation process for winds over background waves.

2. Experiments and analyses

The experiments were performed in the wind–wave tunnel at NASA Wallops Island, which is 1 m wide, 1.25 m high and 20 m long with a water depth d of 0.75 m. A schematic of the tunnel can be found in Huang & Long (1980).

In this tank, waves can be generated by both a paddle and recirculating air. The paddle oscillates about a point 0.6 m from the air-duct entrance. The paddle has a solid section 0.1 m high which is centrally located at the mean water level. Attached to the paddle and located below the solid section is a 0.15 m flexible plastic section which has rows of circular holes cut out. The holes increase in diameter from 20 to 50 mm. The purpose of the plastic section is to provide a simulation of the water-particle velocity profile under deep-water waves which decreases with depth. The paddle is hydraulically powered and is controlled by a servo-motor such that the paddle oscillates along the tank longitudinal axis in response to an analog control signal. Waves can also be generated by wind, which is induced by a fan within a duct system that recirculates air through the test section. Wind speed is controlled by adjusting valves that regulate the amount of air which passes through either a short by-pass duct or the test section.

Paddle-generated waves for this experiment were produced in response to a sinusoidal signal obtained from a signal generator that allowed the drive frequency to be digitally specified to 0.01 Hz. The r.m.s. magnitude of the drive signal was measured by a Hewlett–Packard 3466 A multimeter. During each experiment, the variation of the drive-signal magnitude was less than 0.1%. For convenience, the paddle waves are referred to as background, regular or paddle waves in this paper.

Measurements of surface displacement ζ were made with capacitance wave gauges at four fetches 4.29, 5.82, 8.86 and 13.45 m from the air-duct entrance. At each fetch, surface elevation was measured at 0.25 m to the left and right of the tank centre. The analog signals were digitized at 20 Hz for 54.6 min, which provided 64k data points per probe. Average power spectra S_ζ were computed for each probe by fast Fourier transform of 2048 data points, which were Hamming filtered. Overlap processing of 1024 data points was employed so that the average spectrum for each probe represented 63 measurements with 10/1024 Hz resolution. The standard deviation of r.m.s. surface elevation between probes at fixed fetch was less than 5% of the average value and showed no cross-channel bias, so fetch mean spectra were computed and are reported for each of the four fetches.

Wind speed was computed from Pitot-tube pressure data obtained above the water surface in the centre of the tank at each fetch. Mean wind speed was recorded at 5–7 elevations ranging from 4 to 15 cm above the mean water level. The profiles were approximately logarithmic and thus the law of the wall was used to compute the wind friction velocity u_*.

3. Results

A description of experiment conditions as well as the influence of wind on regular wave growth rate, modulational frequency, and sideband growth rate are presented in this section.

3.1. *Description of experiment conditions*

The experiments reported here consist of 3 paddle (P) cases, 4 wind (W) cases, and 12 combined (C) paddle-plus-wind cases. The sequence for conducting the experiments

Fetch	$(\overline{\zeta^2})^{\frac{1}{2}}$ (cm)	$(\overline{a^2})^{\frac{1}{2}}$ (cm)	$\bar{a}$ (cm)	μ (%)	$\bar{f}$ (Hz)	ν (%)	$\overline{ak}$
				P01W00			
1	0.612	0.869	0.867	5.509	2.017	0.168	0.142
2	0.578	0.831	0.829	6.766	2.017	0.117	0.136
3	0.506	0.791	0.783	13.517	2.017	0.150	0.128
4	0.527	0.768	0.759	15.387	2.017	0.096	0.124
				P02W00			
1	0.672	0.943	0.942	5.612	2.000	0.134	0.152
2	0.663	0.933	0.931	6.574	2.034	0.149	0.155
3	0.611	0.893	0.885	13.405	1.951	0.144	0.136
4	0.615	0.881	0.829	36.007	1.860	0.227	0.115
				P03W00			
1	0.952	1.366	1.362	7.350	2.000	0.227	0.219
2	0.957	1.349	1.344	8.516	2.000	0.156	0.216
3	0.859	1.290	1.267	18.996	1.890	0.205	0.182
4	0.716	1.206	1.166	25.242	1.690	0.267	0.134

TABLE 1. Paddle-generated-wave summary

was as follows. First, each *P*-case was conducted on two separate days so that the repeatability of these conditions could be established. The data showed that the spectral shapes were similar and that the r.m.s. elevation at fixed fetch deviated by less than 1 %. Thus the *P*-cases could be reasonably re-established by resetting the paddle drive controls. *W*- and *C*-cases were conducted by setting the wind controls and then measuring a *W*-case followed by 3 *C*-cases. The tank was always allowed to settle to calm conditions as determined by a spectrum analysis of surface elevation between data runs. Operational conditions were allowed to stabilize for at least 15 min before data acquisition commenced.

The experimental conditions are summarized in tables 1–3. Fetch mean spectra were used to compute spectral moments m_i that yielded root-mean-square surface elevation $(\overline{\zeta^2})^{\frac{1}{2}} = m_0$, and frequency bandwidth ν defined as

$$\nu^2 = \frac{m_0 m_2 - m_1^2}{m_0 m_2}, \tag{3.1}$$

where ζ is surface elevation. In addition to the spectral analysis, a zero-crossing program was employed to obtain the wave amplitude a and wave-period distributions at each fetch. Each distribution contained at least 6500 waves. Moments of these distributions were calculated to obtain mean and r.m.s. wave amplitude, standard deviation μ of wave amplitude, and mean wave frequency $\bar{f}$. Mean wavenumber was computed from the mean wave period by using the deep-water linear dispersion relationship. The mean wave steepness $\overline{ak}$ is the product of the mean wave amplitude and the mean wavenumber.

Paddle-only experiments are identified as P01W00–P03W00, corresponding to increasing r.m.s. elevation, and are summarized in table 1. For the *P* cases, the r.m.s. elevation ranged from 0.612 to 0.952 cm at fetch 1 but decreased owing to dissipation as the waves propagated. The data show that the mean wave frequency at fetch 1 was 2 Hz, which by deep-water linear wave theory yields a wavenumber of 0.161 cm^{-1}. Therefore $kd \gg 1$ and thus deep-water-wave theory is appropriate. Notice

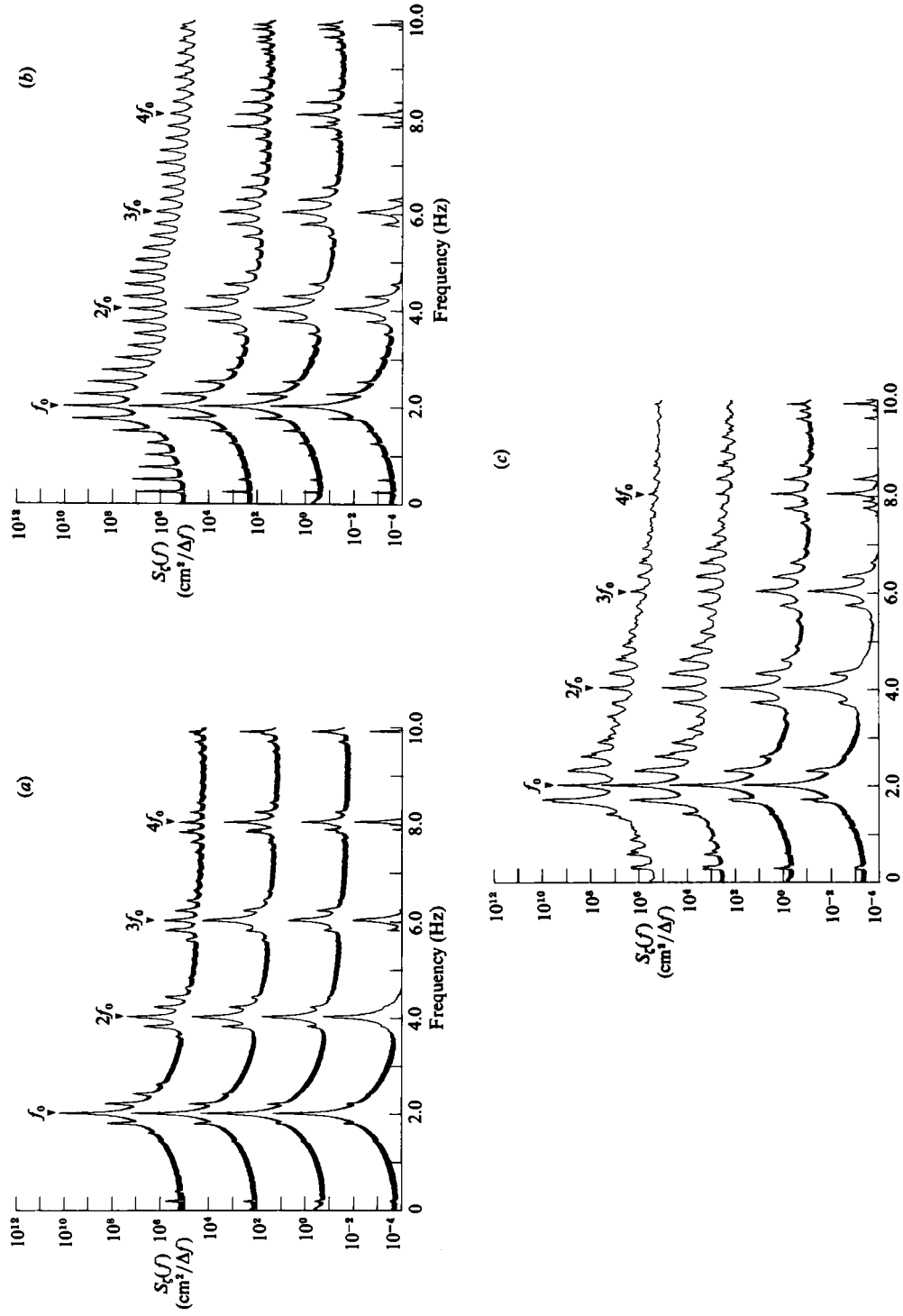

FIGURE 1. Power spectra of paddle-generated-wave surface displacement at $x = 4.29$, 5.82, 8.86 and 13.45 m for (*a*) P01W00, (*b*) P02W00, and (*c*) P03W00. Spectra are sequentially offset by 10^{2n}, $n = 0, 1, 2, 3$. Resolution bandwidth $(\Delta f) = 0.00977$ Hz; Nyquist frequency = 10 Hz; 126 degrees of freedom.

Fetch	$(\overline{\zeta^2})^{\frac{1}{2}}$ (cm)	$(\overline{a^2})^{\frac{1}{2}}$ (cm)	$\bar{a}$ (cm)	μ (%)	$\bar{f}$ (Hz)	ν (%)	$\overline{ak}$	u_* (cm/s)
				P00W01				
1	0.050	0.061	0.055	45.268	6.667	0.286	0.099	14.5
2	0.095	0.098	0.087	52.702	6.316	0.197	0.139	
3	0.181	0.168	0.138	69.609	4.800	0.184	0.128	
4	0.309	0.255	0.195	84.586	3.582	0.208	0.101	
				P00W02				
1	0.094	0.112	0.103	42.788	6.667	0.236	0.185	15.2
2	0.151	0.164	0.148	48.594	5.217	0.194	0.162	
3	0.260	0.249	0.210	62.770	4.211	0.209	0.150	
4	0.420	0.354	0.280	77.489	3.333	0.223	0.125	
				P0W03				
1	0.120	0.143	0.132	43.022	6.486	0.227	0.223	17.5
2	0.188	0.207	0.186	48.810	5.000	0.206	0.188	
3	0.323	0.311	0.264	62.214	4.000	0.217	0.170	
4	0.505	0.433	0.346	75.443	3.000	0.226	0.125	
				P0W04				
1	0.186	0.232	0.214	41.045	5.217	0.220	0.235	25.5
2	0.280	0.320	0.291	45.922	4.444	0.226	0.231	
3	0.450	0.456	0.394	58.031	3.429	0.241	0.186	
4	0.648	0.590	0.488	68.084	2.857	0.229	0.160	

TABLE 2. Wind-generated-wave summary

that the mean wave frequency downshifts at fetch 4 for the P02W000 and P03W00 cases to 1.86 and 1.69 Hz respectively. The variation of wave amplitude indicates that the waves were very regular at fetch 1 with amplitude variation on the order of 5 %. Wave-amplitude variation increases as the waves propagate. The wave steepness at fetch 1 ranged from 0.142 to 0.219.

Background-wave spectra are presented as a function of fetch in figure 1. These are power spectra and so area represents energy units. At fetch 1, the spectra resemble Stokes-wave spectra in that the spectral maximum and its harmonics are prominent features. As the waves propagate down the channel sidebands develop, owing to a low-frequency perturbation, such that (1.1) and (1.2) are approximately satisfied. These sidebands tend to be the dominant sidebands around the spectral peak. Multiple low-frequency-perturbation components at $n(\delta f)$, where $n = 1, 2, 3, \ldots$, become more evident, however, as the initial wave steepness increases and multiple sideband pairs are also present around the dominant wave. These features are also interpreted as type-I instabilities because the spectra show that each dominant-wave sideband pair is associated with a low-frequency perturbation and the resonant condition given by (1.1) is satisfied. At higher frequencies, sidebands are also present around the dominant-wave harmonics. Notice that the frequencies of these sidebands do not correspond to harmonics of the dominant-wave sidebands but, rather, occur at frequencies relative to the harmonic frequency equal to low-frequency perturbations. Thus the type-I instability may be responsible for the sidebands of the harmonics. Sidebands around harmonics of regular waves have been reported by Melville (1982) who attributed the feature to possible interactions between the dominant wave and its harmonics. A more thorough explanation of these features

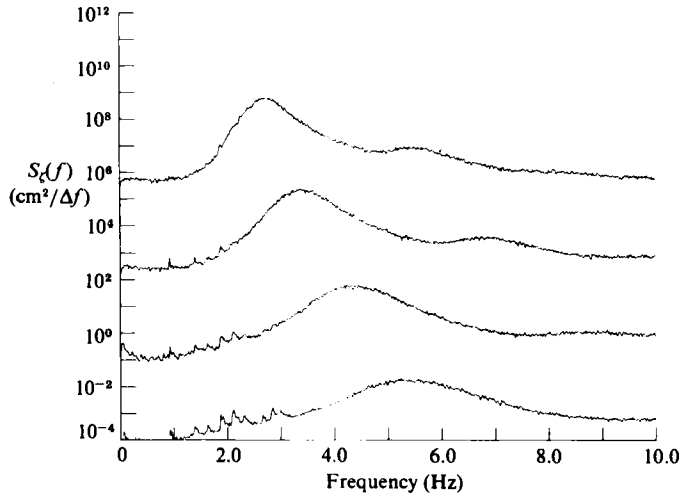

FIGURE 2. Power spectra of wind-generated-wave surface displacement at $x = 4.29$, 5.82, 8.86 and 13.45 m for P00W04. See caption of figure 1 for details.

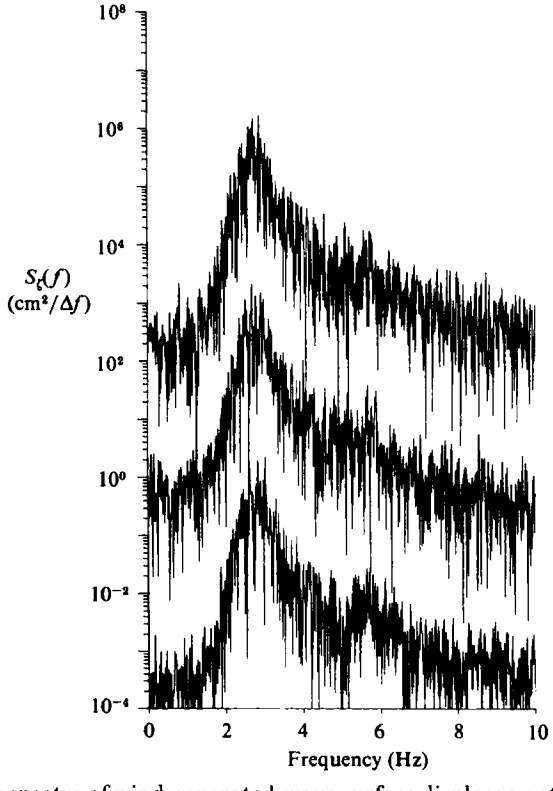

FIGURE 3. Power spectra of wind-generated-wave surface displacement at $x = 13.45$ m for P00W03. Spectra sequentially offset by 10^{3n}, where $n = 0, 1, 2$. Resolution bandwidth = 0.00977 Hz; Nyquist frequency = 10 Hz; and degrees of freedom = 2. Note lack of discernible sidebands even though ak-range for this wind case is similar to P03W00 shown in figure 1.

awaits theoretical development. One final feature shown by figure 1 is that the first harmonic of the spectral peak is normally greater than the other nearby local maxima. At fetch of P03W00, however, the spectral-peak frequency is 1.69 Hz rather than 2 Hz but the harmonic of the 2 Hz component is still the local maximum.

The wind-only cases are summarized in table 2 and are labelled P00W01–P00W04, corresponding to increasing wind friction velocity. Friction velocity at fetch 1 ranged from 14 to 25 cm s^{-1} yielding mean frequencies of 6.66 and 5.2 Hz and elevation variation of 0.050–0.186 cm (r.m.s.) at that fetch. The mean wave slope of the wind waves at fetch 1 ranged from 0.099 to 0.235, which corresponds to the range produced by the paddle drive, but the amplitude variations and spectral widths of the wind waves are greater than for the paddle waves. The lowest peak frequency measured for the wind-wave cases is 2.9 Hz for P00W04 at fetch 4, so the energy-containing wind-wave frequencies do not overlap the dominant paddle-wave frequency.

A typical sequence of wind spectral development with fetch is shown in figure 2, which shows energy growth and frequency downshifting for the highest wind case. What evidence is there for type-I instabilities in the wind-wave spectra? Although the spectra exhibit some low-frequency local energy maxima at frequencies less than the spectral peak, these low-frequency energy bands develop differently from those observed for the *P*-cases. In particular, they decay, rather than grow, with fetch and also no sidebands relative to the spectral peak at frequency differences corresponding to the low-frequency perturbations are apparent. Thus evidence that they are associated with a type-I instability is lacking.

Type-I instabilities are evident in the *P*-spectra but are not present in the *W*-spectra and so we produced spectra from shorter time records of *W*-data to assess whether spectral averaging has smoothed out the sidebands. Figure 3 shows a waterfall display of spectra based upon 102 s of data for the wind P00W03 case at fetch 4. This case was chosen because ak varied from 0.223 to 0.125 for fetches 1 and 4 respectively. This initial slope is much greater than 0.1, which may be considered as the minimum steepness required for instability development by regular waves. This ak-range is also similar to the regular-wave case P03W00 whose spectra showed clearly defined sideband development. Finally, fetch 4 was chosen because the regular-wave cases show that, owing to the exponential growth of the sidebands, sidebands are more easily observed as fetch increases. Because the mean frequency for this case is 3 Hz, 102 s represents approximately 300 waves, which corresponds to 50 wave groups if one assumes an average of 6 waves per group. Thus 102 s should provide ample duration to resolve sidebands from noise. Given all these considerations, the wind–wave spectra in figure 3 do not exhibit type-I instability features that can be resolved from the variation in spectral-energy density associated with the limited degrees of freedom. Thus we conclude that spectral averaging has not smeared the wind-wave spectra concealing type-I instabilities.

Data have been presented by Hatori (1984) to show that wind-wave-frequency downshifting is due to the type-I instability process. He presented wind-wave spectra from one-hour data records obtained in a wave tank for u_* values of 27.2, 45.9 and 63.5 cm s^{-1}. For high wind speeds he claimed that data sets show sidebands which satisfy the resonance condition given in (1.2). These features, however, diminished as friction velocity decreased such that, for the 27.2 cm s^{-1} data, the features were 'not seen so clearly'. Although in the discussion he states that one possible mechanism responsible for the resonance-frequency condition is the type-I instability, no further evidence was presented to verify that the observed features were indeed due to type-I instabilities. For example, only figure 2 of that paper is in a format that permits

Fetch	$(\overline{\zeta^2})^{\frac{1}{2}}$ (cm)	$(\overline{a^2})^{\frac{1}{2}}$ (cm)	$\bar{a}$ (cm)	μ (%)	$\bar{f}$ (Hz)	ν (%)	$\overline{ak}$	u_* (cm/s)
				P01W01				
1	0.581	0.826	0.821	11.460	2.017	0.257	0.134	16.1
2	0.572	0.839	0.833	12.491	2.000	0.303	0.134	
3	0.623	0.873	0.859	17.930	2.000	0.309	0.138	
4	0.724	0.913	0.890	23.106	2.000	0.258	0.143	
				P01W02				
1	0.619	0.889	0.883	11.952	2.000	0.281	0.142	16.6
2	0.643	0.935	0.928	12.351	2.000	0.315	0.149	
3	0.725	0.984	0.966	19.383	2.000	0.277	0.155	
4	0.855	1.043	1.016	23.225	2.000	0.238	0.164	
				P01W03				
1	0.623	0.907	0.897	15.106	2.000	0.314	0.144	19.5
2	0.668	0.969	0.961	13.516	2.000	0.303	0.155	
3	0.757	1.040	1.018	20.603	2.000	0.284	0.164	
4	0.918	1.117	1.085	24.564	2.000	0.237	0.175	
				P01W04				
1	0.647	0.925	0.886	30.307	2.000	0.338	0.143	25.2
2	0.757	1.086	1.045	28.225	2.000	0.308	0.168	
3	0.907	1.258	1.238	17.976	2.000	0.262	0.199	
4	1.230	1.466	1.421	25.278	2.000	0.230	0.229	
				P02W01				
1	0.695	0.996	0.993	8.452	2.017	0.252	0.162	16.3
2	0.739	1.022	1.016	10.755	2.017	0.261	0.166	
3	0.764	1.042	1.031	14.794	2.000	0.267	0.166	
4	0.869	1.087	1.072	17.104	2.000	0.223	0.172	
				P02W02				
1	0.755	1.076	1.071	9.400	2.017	0.248	0.175	17.1
2	0.777	1.116	1.109	11.442	2.000	0.293	0.178	
3	0.873	1.168	1.157	14.237	2.000	0.236	0.186	
4	1.008	1.253	1.224	21.887	2.000	0.223	0.197	
				P02W03				
1	0.796	1.118	1.112	10.555	2.000	0.234	0.179	20.7
2	0.828	1.177	1.169	11.236	2.000	0.270	0.188	
3	0.934	1.252	1.237	15.229	2.000	0.237	0.199	
4	1.159	1.389	1.353	23.133	2.000	0.219	0.218	
				P02W04				
1	0.792	1.152	1.130	19.796	2.000	0.314	0.182	29.4
2	0.917	1.301	1.281	17.751	2.000	0.257	0.206	
3	1.129	1.495	1.466	19.867	2.000	0.277	0.236	
4	1.430	1.679	1.622	26.864	2.000	0.251	0.261	

TABLE 3. Paddle- plus wind-wave summary. Part I.

examination for low-frequency-perturbation components. For the case presented, no low-frequency perturbations corresponding to the spectral-peak sidebands can be observed. Furthermore, no evidence demonstrating a relationship between normalized sideband frequency and steepness as predicted by type-I instability theory was presented but, rather, the normalized sideband frequency was approximately constant and equal to 0.1. Finally, sideband growth rates were not computed and compared with theoretical predictions. Thus the limited evidence that was presented does not seem to demonstrate that the features that were observed were necessarily a result of a type-I instability mechanism. The maximum wind friction velocity that we report

Fetch	$(\overline{\zeta^2})^{\frac{1}{2}}$ (cm)	$(\overline{a^2})^{\frac{1}{2}}$ (cm)	$\bar{a}$ (cm)	μ (%)	$\bar{f}$ (Hz)	ν (%)	$\overline{ak}$	u_* (cm/s)
				P03W01				
1	0.953	1.392	1.388	7.296	2.000	0.269	0.223	17.8
2	1.010	1.441	1.436	8.425	2.000	0.243	0.231	
3	1.085	1.474	1.460	13.930	1.967	0.201	0.227	
4	0.952	1.393	1.338	29.025	1.778	0.309	0.170	
				P03W02				
1	1.025	1.486	1.482	7.500	2.000	0.252	0.238	23.8
2	1.121	1.541	1.535	8.733	2.000	0.175	0.247	
3	1.200	1.620	1.605	13.713	2.000	0.218	0.258	
4	1.134	1.577	1.530	24.849	2.000	0.286	0.246	
				P03W03				
1	1.066	1.533	1.528	7.644	2.000	0.244	0.246	26.4
2	1.169	1.609	1.601	9.449	2.000	0.195	0.258	
3	1.298	1.722	1.705	14.133	2.000	0.231	0.275	
4	1.318	1.741	1.706	20.592	2.034	0.264	0.284	
				P03W04				
1	1.123	1.588	1.568	16.216	2.000	0.218	0.252	33.7
2	1.257	1.786	1.769	13.587	2.000	0.218	0.285	
3	1.472	1.998	1.974	15.663	2.000	0.244	0.318	
4	1.466	1.961	1.926	19.361	2.000	0.269	0.310	

TABLE 3. Paddle- plus wind-wave summary. Part II.

for fetch 1 for the wind-only cases was 25.2 cm s^{-1} so the lack of sidebands is consistent with data presented by Hatori. We concentrated our study on lower wind friction velocities so that the ratio of the wind friction velocity to wave phase speed would be small and thus be more representative of conditions that are likely to be observed in the field. Whereas our wind-wave spectra show no evidence of the type-I instability mechanism, further experiments and analysis are needed to clarify the role of the type-I instability mechanism for wind waves at higher wind friction velocities.

Having described the separate features of paddle and wind waves, we present a summary of the *C*-conditions in table 3. The experiment labels correspond to the paddle and wind conditions that were reported previously. Elevation data show that total wave energy grew with fetch owing to the input of energy from the wind. Slope values ranged from 0.134 to 0.318. Whereas the mean frequency of the P02W00 and P03W00 cases downshifted as the waves propagated, except for the lightest-wind, steepest-paddle case (P03W01), the addition of wind stopped the frequency downshifting. The amplitude variation of the *C*-cases was typically greater than the corresponding *P*-case and tended to increase as wind speed increased, but the maximum *C*-value of 25% is considerably less than the minimum value of 40% recorded for the *W*-cases. The friction-velocity data in table 3 reveal the influence of background waves on friction velocity for the conditions reported here. The data show that, for a fixed fan setting, as the background-wave steepness increased the friction velocity increased. For example, the friction velocity for the P03 case increased from 18 to 34 cm s^{-1} as ak at fetch 1 increased from 0.223 to 0.252. Thus, for these cases, air friction velocity increased as background wave steepness increased.

A brief description of the wavefield appearance follows. Visual observations of the wavefield were made through the glass sidewall, but down/up channel photography

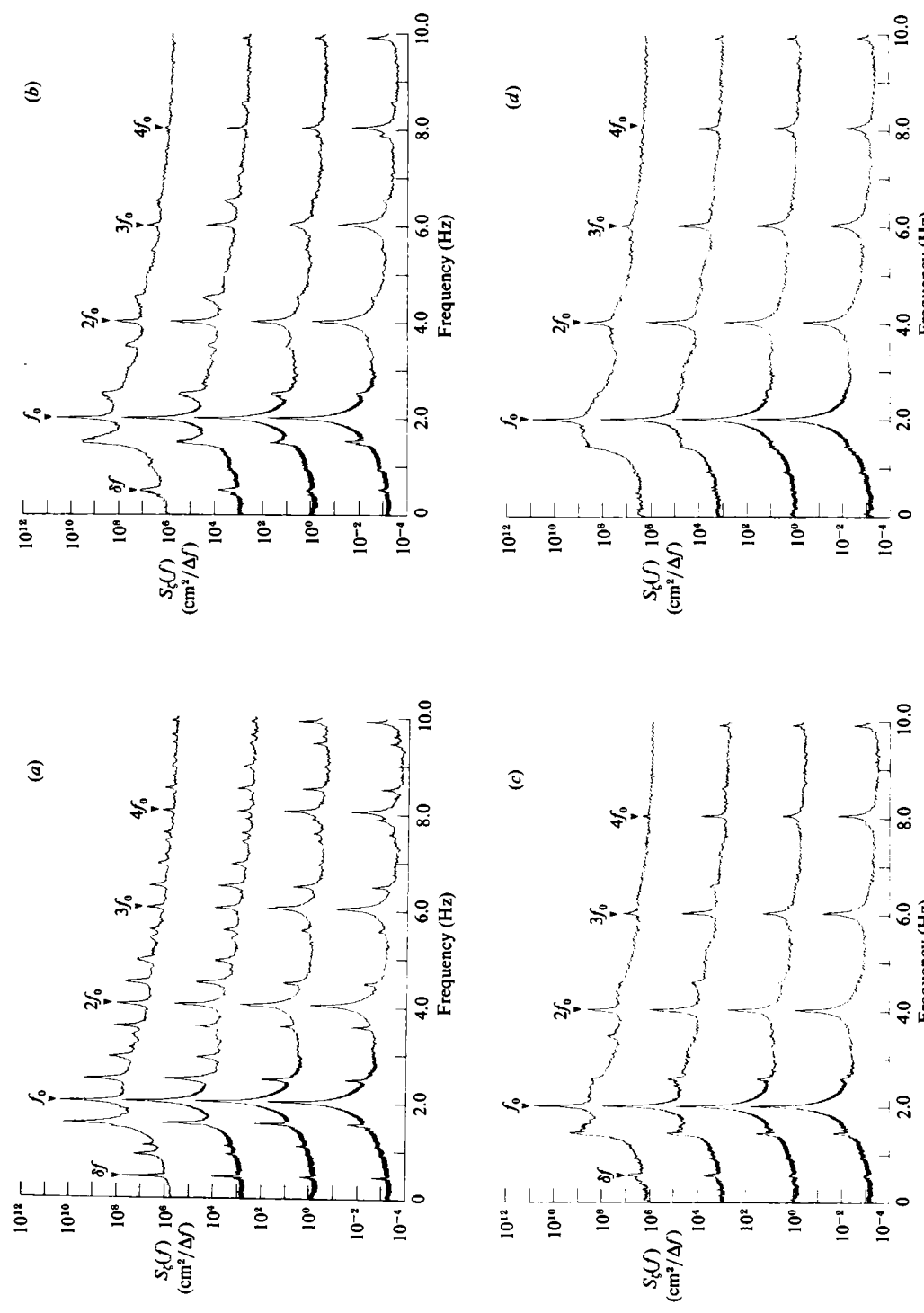

FIGURE 4. Power spectra of combined paddle-plus-wind generated wave surface displacement at $x = 4.29$, 5.82, 8.86 and 13.45 m for (*a*) P03W01, (*b*) P03W02, (*c*) P03W03, and (*d*) P03W04. See caption of figure 1 for details.

of the wavefields during these experiments was not attempted because of the necessity of keeping the opaque top of the tank closed in order to maintain the wind field. For paddle-generated waves, the transition from two- to three-dimensional breaking seems to be related to wave steepness and non-dimensional fetch. Melville (1982) using a 28 m long tank found that, for paddle waves, type-I instabilities occurred for $ak < 0.29$ but for $ak > 0.31$, three-dimensional instability dominated. Su *et al.* (1982), however, using both a 137 m long tank and a 1500 m long basin, obtained three-dimensional wavefields for $0.25 < ak < 0.34$. In the present study, the paddle-generated waves all appeared two-dimensional up to the breaking point. Breaking was gentle with only occasional bubble generation. Wind waves were three-dimensional with considerable cross-channel amplitude variations, but the breaking was still gentle with not much bubble production. Although the 2 Hz wave frequency is dominant in the spectra of the *C*-cases, the wavefield appeared three-dimensional for all cases owing to small-scale waves. The dominant waves were breaking with occasional bubble entrainment. This experiment was not designed to characterize wave breaking so a more detailed breaking description seems inappropriate, particularly considering the complex nature of the paddle-plus-wind wavefields.

3.2. *Wavefield evolution for winds over background waves*

This section presents typical characteristics of the *C*-spectra, the deviation of *C*-spectra from linear superposition of *P*- plus *W*-spectra, and the relative modification of *C*-spectral components.

Example spectra for the *C*-cases are presented in figure 4, which shows the spectral sequence for the steepest paddle waves subject to increasing wind. Comparisons of the *C*-spectra relative to the *P*-spectra reveal that the dominant features that these graphs display are the reduction of magnitude of the sidebands as wind speed increases and the broadening of energy in the frequency band between the sidebands around the spectral peak. For each fetch, one can see that the magnitude of the sidebands decreases as the wind speed increases. Moreover, at fetch 4 for the P03W00 case where the peak wave frequency had downshifted to the frequency of the lower sideband, the winds reduced the magnitude of the sidebands sufficiently so that the 2 Hz wave remained as the spectral peak. For the high-wind case, P03W04, note the lack of distinguishable sidebands. The combined spectra also exhibit the influence of wind on the low-frequency-perturbation components which are suppressed as wind speed increases. The suppression is such that, by P03W04, no low-frequency perturbation that can be associated with a sideband near the spectral peak can be identified. Thus the role of the type-I-instability mechanism for frequency downshifting for the P03W04 case is unclear. This trend of suppression of the perturbation-frequency components and sidebands is consistent with the observed lack of low-frequency-perturbation components and sidebands in the wind-wave spectra.

To further demonstrate the decay of the lower sideband at a fixed fetch as the wind speed increased, figure 5 was constructed from the P03 data. For each of the 4 fetches, the graph shows the *C* lower-sideband magnitudes normalized by the lower-sideband magnitude of the corresponding P03W00 value as a function of $(u_*/c_0)^2$. The parameter $(u_*/c_0)^2$ was used because it quantifies the wind friction velocity relative to the wave phase speed c_0 and thus is a measure of the potential for energy transfer from the air to the waves (Huang *et al.* 1985). The graph shows the rapid decay of the sideband as $(u_*/c_0)^2$ increases. Thus, as the wind becomes stronger, the magnitudes of the sidebands at a given fetch are reduced.

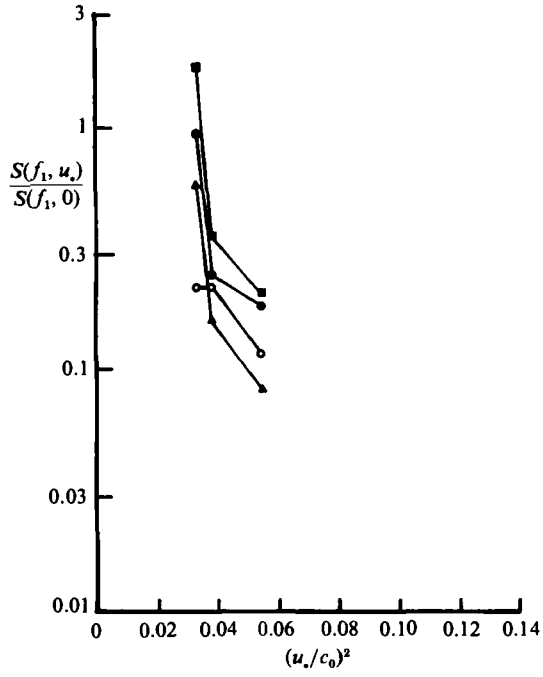

FIGURE 5. Decay of lower-sideband-energy density as wind speed increases: ○, fetch 4.29 m; ●, 5.82 m; ▲, 8.86 m; ■, 13.45 m.

Spectral-energy composition of the C-cases is reported next in order to characterize the wind-to-wave energy-transfer process. Deviations from linear superposition that occur for combined wave conditions with positive/negative values representing excess/deficit energy transfer were obtained by computing the difference between C-spectra minus the sum of the corresponding P- and W-spectra. These spectral differences, which are in energy-density units, illustrate the modification of wind-wave generation due to the presence of background waves. Typical results are exhibited in figure 6, which shows the P03W04 case. Linear vertical and horizontal axes are used so that equal-area units represent equal energy and thus comparisons among frequency bands is facilitated. This sequence shows that in physical units the dominant effect is an excess energy transfer to the background-wave frequency. The transfer of momentum from the wind to the wavefield has been studied in depth by Hatori, Tokuda & Toba (1981) and found to be a function of both the background-wave steepness and the ratio of the frequency of the background wave to the frequency of the wind wave in the absence of a background wave. Although the waves studied here are much steeper than those reported in that study, the energy transfer to the background waves that we report would be expected from an extrapolation of the earlier results. Frequency down/upshifting of the sidebands can also be observed in figure 6 for the fetch 4 data and is discussed further in §3.3.

What is the mechanism for transferring energy to the 2 Hz dominant waves for these combined cases? Although this experiment was not designed to assess the growth mechanism for the background waves, it is possible to qualitatively assess the likely mechanisms. The spectra we report are rather narrow-banded around the spectral-peak frequency so that nonlinear transfer of energy should be ineffective as

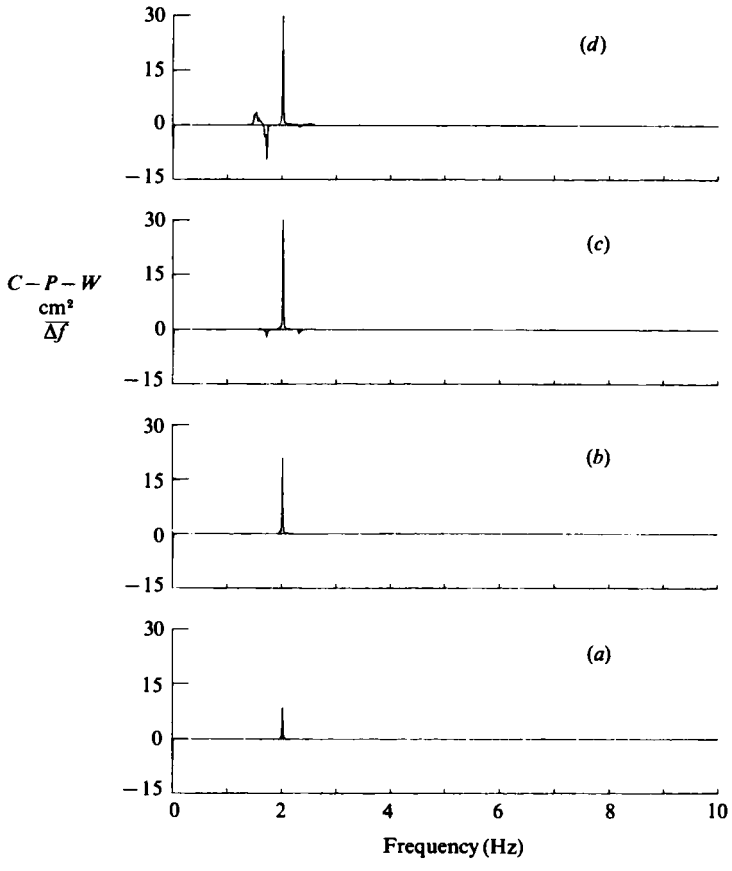

FIGURE 6. Surface-displacement power-spectral difference ($C-P-W$) at x = (*a*) 4.29, (*b*) 5.82, (*c*) 8.86 and (*d*) 13.45 m for P03W04. These differences represent the deviation from linear superposition for combined conditions as compared to background plus wind waves. Note that, for combined conditions, the background 2 Hz wave frequency receives the dominant wind-energy input and that at x = 13.45 m the sideband frequency down/upshifting can be observed.

a mechanism for high-frequency to low-frequency energy conversion. Plant (1982), however, has presented an expression for spectral-energy growth rate β for direct energy transfer from wind to wave components as

$$\beta = \frac{(0.04 \pm 0.02)\, u_*^2\, \omega \cos\theta}{c^2}, \tag{3.2}$$

where ω is the radian frequency and $\cos\theta$ is the angle between the wind and the wave component. Plant found maximum deviation from this equation to occur for (i) waves longer than 10 cm, (ii) waves travelling at or near the wind speed, and (iii) for waves near 20 Hz. A further recommendation was that (3.2) should not be used for conditions including background waves at random angles. Mitsuyasu & Honda (1982) later found that the square-law growth rate also provides a reasonable fit for the growth rate of mechanically generated waves with wavelengths of 56–263 cm under the influence of wind. The proportionality constant that they computed by a least-square fit of their data was at the upper limit of that proposed by Plant (1982). We computed the growth rate of the 2 Hz wave component for the combined cases,

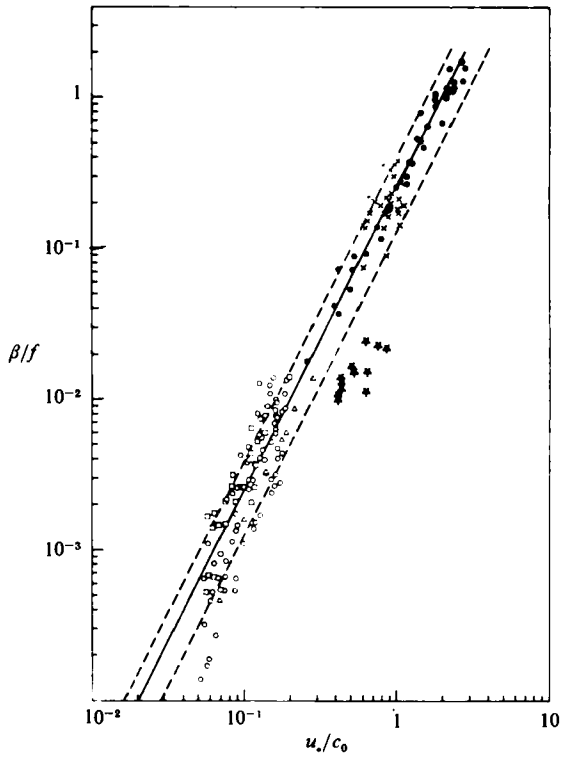

FIGURE 7. Wind-induced growth rate β normalized by wave frequency *versus* friction velocity per unit phase velocity as summarized by Plant (1982): ——, – – –, (3.2); △, Shemdin & Hsu (1967); ●, Larson & Wright (1975); ×, Wu, Hsu & Street (1977, 1979); ○, Snyder *et al.* (1981), fixed sensors; □, Snyder *et al.* (1981), wave-following sensor; ★, this study.

allowing for surface damping and boundary dissipation at sidewalls and tank bottom according to theories proposed by Lamb (1932) and Hunt (1952). These theories provided close agreement with the tank data generated by Mitsuyasu & Honda (1982) and so should provide an adequate estimate for our data. Normalized growth rates (β/f) of the 2 Hz background wave as a function of u_*/c_0 for our data have been incorporated into the growth-rate diagram presented by Plant (1982) and are shown here in figure 7. The data show that the growth rate for the background waves agrees well with a square-law dependence on u_*/c_0 but that the constant of proportionality is slightly less than that computed by Plant. Thus the data seem to indicate that the background-wave growth was due to direct transfer of energy from the wind. The exponential-growth-rate model proposed by Plant (1982) appears to offer a simple explanation for the selectively rapid growth of the background waves that we observed, since this model favours the growth of those components with large initial amplitudes and low frequencies. This can be shown easily from (3.2) by combining the phase velocity and the frequency terms to produce a single inverse frequency-dependent growth rate for any wave component.

The spectral-energy-density magnitude for each of the C-cases varies over several decades, so a measure of the relative change of each spectral component was examined to assess the departure of the C-conditions from the sum of the P- plus W-values. Thus the C-spectra were normalized by the sum of the P- and W-spectra. This representation quantifies the relative change of each frequency component. A typical

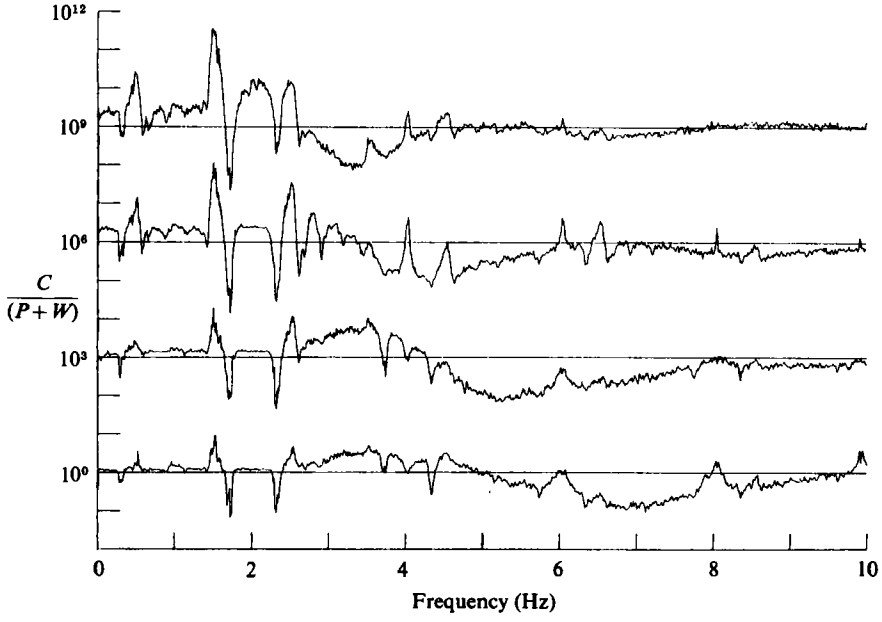

FIGURE 8. Surface-displacement power-spectral ratios $C/(P+W)$ at $x = 4.29, 5.82, 8.86$ and 13.45 m for P03W04. Data at fetches sequentially multiplied by 10^{3n} ($n = 0, 1, 2, 3$) and the axis of ordinates is logarithmic. These ratios represent the combined conditions with respect to background-plus-wind conditions and illustrate the relative change of the spectral components. Note frequency shift of sidebands, background-wave primary and harmonics energy growth, and wind-wave-energy deficit.

result is shown in figure 8 for case P03W04 in which excess/deficit normalized energy transfers are greater/less than one. The vertical axis is logarithmic in order to permit observation of detailed characteristics in the large dynamic range of values. Several distinct features can be identified in this graph. First, the background-wave energy is enhanced by the wind but what is new is that the harmonics of the background wave are also preferentially receiving energy. Therefore the background-wave profile under the action of wind becomes more skewed as a result of growth of harmonics. Of course this feature would ultimately be limited by wave breaking. Figure 8 also shows a deficit of energy at the wind–wave frequencies, which is consistent with observations of wind-wave and swell conditions by Banner & Phillips (1974), Hatori *et al.* (1981), and Imai *et al.* (1981). Two different theoretical models of this wave-energy reduction have been proposed by Phillips & Banner (1974) and Imai *et al.* (1981), and further investigation is needed to clarify when each is applicable. A final dramatic feature of figure 8 is the frequency up/downshifting of the sidebands, which is discussed further in the following section.

3.3. *Modulational frequency*

A characteristic feature of steep-regular-wave evolution is the onset of type-I instability, which is usually modelled by prediction of the normalized modulation frequency as a function of the wave steepness. The Benjamin–Feir analysis is asymptotic for $ak \to 0$. Finite-amplitude effects were incorporated in an analysis of Zakharov's equation by Crawford *et al.* (1981) in order to improve the agreement between experimental data (Lake & Yuen 1977) and theory for steeper wave conditions. Later, Melville (1982) employed finite-amplitude instability results

derived by Longuet-Higgins (1978) to further extend the range of validity and to account for the asymmetric sideband growth rates.

These analytic relationships between the normalized modulation frequency versus wave steepness were derived for free waves and supported by paddle-generated-wave data. To assess the influence of wind on the relationship between the modulation frequency and $\overline{ak}$, the normalized modulation frequency and wave-steepness values were obtained from our experimental data. Two techniques have been previously employed to estimate the modulational frequency. The technique that Lake & Yuen (1978) employed was based upon zero crossings and wave amplitudes to determine the number of waves in a group. An alternative method, which will be called the spectral method, is usually employed for paddle waves. The frequencies of sidebands are clearly defined in frequency spectrum of free regular waves. Thus the ratio of the sideband and spectral-peak frequencies is used to compute the normalized modulational frequency. The spectral method was employed here to ensure that the type-I instability mechanism was being assessed. It should be emphasized that it is usually not possible to identify sidebands in wind-wave spectra and thus it is not possible to be sure that the modulation is a result of a Benjamin–Feir-type instability. In this study, however, the *C*-conditions represent steep paddle-waves plus light winds, so that in some cases the sidebands could be identified and the modulational frequency assessed as a function of the wave steepness. The modulation frequency was determined from tables of the spectral-density values, which were compared to graphs of the spectra, and when possible, the lower-sideband frequency was obtained at fetch 4. These lower-sideband frequencies were divided by the mean wave frequency at fetch 4 to produce the normalized modulation frequency. Data from fetch 4 were used because the sideband frequency is constant for considerable distances but sidebands grow with fetch and so they are most easily identified at longer fetches. It was not possible to determine sideband frequencies for the combined P01 series because of sideband suppression. P02W03, P02W04, and P03W04 were excluded owing to sideband broadening. Wave steepness is referenced to upstream conditions at fetch 1 because the analysis is an initial-value problem.

Figure 9 shows the variation of normalized modulational frequency with respect to wave steepness as the wind stress was increased over P02 and P03. The graph includes for comparison the theoretical predictions by Benjamin & Feir (1967) and Longuet-Higgins (1978, 1980). The modulational frequencies for the *P*-cases are less than the theories predict but are generally within the range that was observed by Lake & Yuen (1977). The data in figure 9 show that, as the wind stress increased, the modulational frequency increased proportionately more rapidly than the wave steepness. Although the normalized modulation frequency for combined conditions has the same order of magnitude as predicted by the Longuet-Higgins' analysis, the positive bias seems large enough, considering previous data for paddle-generated waves, that perhaps a two-parameter model consisting of wave steepness and u_*/c_0 could improve the prediction accuracy. In summary, the data seems to indicate that, for combined conditions, the normalized modulational frequency determined from identifiable sidebands is greater than would be expected from considering only wave steepness.

3.4. *Sideband growth rates*

Type-I instabilities for regular waves have been shown to grow at an exponential rate for free regular waves (see for example Lake *et al.* 1977 and Melville 1982). Now we will discuss the influence of wind on the growth rate of type-I instabilities.

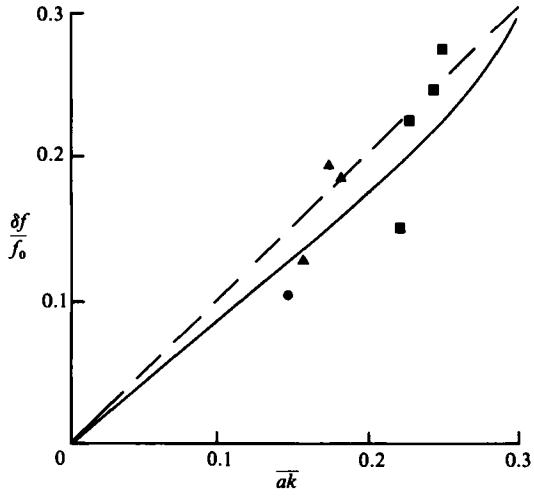

FIGURE 9. Normalized modulation frequency $\delta f/f_0$ *versus* $\overline{ak}$. ---, Benjamin & Feir (1967); ——, Longuet-Higgins (1978, 1980). ●, P01; ▲, P02; and ■, P03. Values less than Longuet-Higgins' theory are *P*-cases. Other values are *C*-cases,

Growth rates were estimated by a procedure similar to that employed by Lake & Yuen (1977) and Melville (1982). This technique employs the ratio of energy densities of the sideband to the spectral peak to define the normalized sideband energy. Growth rates are determined using an exponential model of the non-dimensional sideband magnitude as a function of non-dimensional fetch. The influence of dissipative mechanisms on growth-rate estimates determined by this technique needs to be considered. Although this procedure may remove first-order effects of dissipation mechanisms because the sideband and the primary are approximately the same frequency, the influence of specific dissipative processes on the growth rates cannot be accurately estimated for several reasons. Miles (1967) showed that it is not possible to make accurate determinations for dissipation from causes other than breaking, such as viscous dissipation at the boundaries, surface contamination, capillary-wave generation and capillary hysteresis, because all these mechanisms produce monotonic decreases. Melville reported that another disadvantage of the method when applied to steep regular waves is that the amplitude of the fundamental does not decrease monotonically but, rather, displays a maximum and a minimum that are associated with wave breaking. Given these considerations, we employ the technique here in order to provide a qualitative presentation of the influence of wind on sideband growth rates and also to present results in a manner consistent with previous results in the literature.

The influence of wind speed on normalized sideband growth rates is shown in figure 10. The growth rates were determined as follows. Normalized sideband energy, which is the ratio of the lower-sideband to peak-power-spectral-density values, was computed from values obtained from tables of the power-spectral-density values. An exponential model of the normalized sideband energy to non-dimensional fetch was computed by a least-squares technique for each wind and paddle case. The exponential model that was employed is given by

$$\frac{S_\zeta(f_0-\delta f)}{S_\zeta(f_0)} = \alpha \exp(\gamma \tilde{x}), \tag{3.3}$$

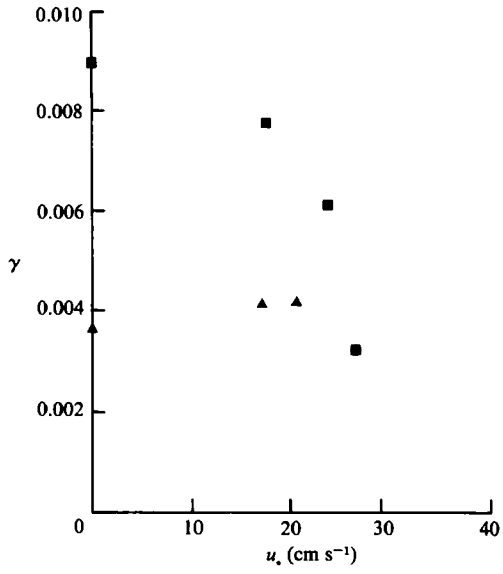

FIGURE 10. Sideband growth rate as a function of wind friction velocity: ▲, P02; and, ■, P03. Note that the growth rate increases as ak increases for the paddle-only cases but that the growth rate tends to decrease as wind speed increases even though the wave steepness is increased by the wind.

where α is a constant, γ is growth rate and $\tilde{x}$ is non-dimensional fetch (xg/u_*^2). Each regression represents data obtained at the four observation fetches, and the correlation coefficients (r^2) for these regressions ranged from 0.82 to 0.99 with a mean of 0.92. Cases were excluded in which the sidebands were not identifiable owing to either suppression or broadening. The free regular-wave cases P02W00 and P03W00 depict higher growth rates as wave steepness at fetch 1 increased from 0.152 to 0.219. Wind forcing dramatically altered this trend. Consider each background-wave case separately. The P02 paddle-plus-wind cases presented in figure 10 had wave steepness at fetch 1 ranging from 0.175 to 0.182 as u_* increased from 17 to 30 cm s^{-1}, but the growth rate remained almost constant. The P03 paddle-plus-wind cases had wave steepness at fetch 1 ranging from 0.223 to 0.252 as u_* increased from 18 to 34 cm s^{-1}, but the growth rate decreased by approximately 50 %. Thus the influence of wind on the sideband growth rates was to retard or diminish the values.

4. Discussion

A series of laboratory experiments have been conducted to investigate the influence of wind on type-I instabilities. Background paddle-generated waves consisted of three cases of steep ($0.14 < \overline{ak} < 0.22$) regular waves with their spectra clearly exhibiting sidebands that grew as the waves propagated down the channel. These spectra displayed local maxima at low frequencies that are perturbation frequencies associated with sidebands around the spectral peak. The magnitude of the perturbation components increased with increasing fetch. Wind-wave cases with air friction velocity of 14–25 cm s^{-1} generated waves with slopes comparable to the paddle-generated waves. Wind-wave spectra, however, did not exhibit sidebands. Although

low-frequency local maxima were sometimes visible in the wind-wave spectra, they decayed with fetch and could not be associated with sidebands.

Combinations of the paddle-plus-wind conditions revealed the influence of wind on type-I instabilities. Data showed that the sideband growth rate decreases as wind speed increases. Spectra at fixed fetches showed that, as wind speed increases, sideband energy decreases but a broad range of frequencies near the carrier frequency gain energy. This process transforms regular-wave spectra into spectra that resemble wind-wave spectra, which are more broad-banded than regular-wave spectra and generally do not exhibit sidebands. Wind over regular waves also suppressed the energy of low-frequency perturbation components that stimulates the instability mechanism responsible for the formation of sidebands.

The sideband-growth-rate reduction we observed may be due to increased bandwidth associated with wind forcing (Alber 1978; Crawford *et al.* 1980), which may cause detuning. Further experiments are needed to resolve the details but our data provide evidence that the influence of wind on regular-wave evolution is to suppress sidebands and their growth rate. In order to make further progress, experiments must be designed to investigate the nature of specific effects on various instability mechanisms.

Other spectral-evolution results from this study do indeed show characteristics which have been observed in previous investigations. Examples of features that can be found in the literature are as follows. Figure 6 of Phillips & Banner (1974) shows spectra for wind and paddle conditions in which the steepest paddle wave had ak equal to 0.175, which is much greater than 0.1, so one might expect to see sidebands. No sidebands are present! Sideband growth for regular waves was similar to results presented by Melville (1982) and the characteristics of the NASA tank closely resembled those described by Melville for the Scripps tank. Combined regular-waves plus wind-waves evolution was similar to past studies by Phillips & Banner (1974), Mitsuyasu & Honda (1982), and Hatori *et al.* (1981). In general the spectral evolution is a function of the slope of the background wave as well as the frequency of the background wave relative to the original wind-wave peak frequency. When ak is sufficiently high, or as the frequency difference decreases, the wind energy is transmitted to the regular-wave component at the expense of the wind-wave components and spectra undergo broadening with fetch until they ultimately resemble wind-wave spectra. For the limited fetches available in our laboratory, however, the steep-regular-wave spectra were transformed to spectra with a broad shoulder and a peak at the preexisting background peak frequency. We also did not observe the new type of instability as suggested by Tsimring (1983) for wind–wave systems.

The results of this experiment also led us to consider the implications of pre-existing wave conditions on the wind-wave-generation problem. Wind-wave-generation theories usually assume an initially calm water surface, but in nature there are many occasions when the initial condition deviates from a calm surface. Background waves can be from sources such as swell propagating into the region or wind-waves propagating from a nearby bay being refracted as they propagate offshore. Regier & Davis (1977) employed an array of probes to measure open-ocean waves from the Research Platform FLIP. From a one-month database, they concluded that a wave spectrum under typical oceanic conditions is not solely determined by local winds but rather is the result of temporal and spatial history. Field studies by Walsh *et al.* (1982) and Jackson (1984) for the fetch-limited wind-wave condition near Delaware Bay showed the persistence of wave components that were radiating from the bay.

These findings substantiate the crucial importance of the initial condition for the wind-wave-generation problem.

Finally, nonlinear coupling of the wind and wavefield demonstrated in these experiments may have serious implications in other air–sea interaction problems. First is the parametrization of wind stress. Wind data collected during these experiments showed that a preexisting wavefield can have a significant influence on the wind field, which we reported in Huang *et al.* (1985). Because the background waves received the bulk of the input wind energy, they also offer the appropriate amount of resistance. Consequently, in the wind-stress-parametrization scheme, the wave conditions exert a non-negligible role. Unfortunately, the influence of waves is sometimes not included in wind-friction-velocity models, which may be a reason for the large scatter in plots of drag coefficient versus wind speed.

The second problem associated with the nonlinear coupling is the influence on remote-sensing applications to the ocean. A common way to remotely sense wind speed is to relate the radar-backscatter coefficient to wind speed by power-law regression analysis (see, for example, Thompson, Weissman & Gonzalez 1983). Our data show that background waves can cause profound modification of small-scale wind-wave generation, as has been previously reported by Mitsuyasu (1966), Phillips & Banner (1974), and Hatori *et al.* (1981). Consequently, the relationship between wind stress and surface roughness needs further investigation. A clearer understanding of this complex situation will require a more complete study of the nonlinear feedback mechanism between wind and waves.

This work was supported in part by NASA contract NAS6-2940.

REFERENCES

ALBER, I. E. 1978 The effects of randomness on the stability of two-dimensional surface wave trains. *Proc. R. Soc. Lond.* A **363**, 525–546.

BANNER, M. L. & PHILLIPS, O. M. 1974 On the incipient breaking of small scale waves. *J. Fluid Mech.* **65**, 647–656.

BENJAMIN, T. B. & FEIR, J. E. 1967 The disintegration of wave trains on deep water. Part 1. Theory. *J. Fluid Mech.* **27**, 417–430.

CRAWFORD, D. P., SAFFMAN, P. G. & YUEN, H. C. 1980 Evolution of a random inhomogeneous field of nonlinear gravity waves. *Wave Motion* **2**, 1–16.

CRAWFORD, D. R., LAKE, B. M., SAFFMAN, P. G. & YUEN, H. C. 1981 Stability of weakly nonlinear deep-water waves in two and three dimensions. *J. Fluid Mech.* **105**, 177–191.

HASSELMANN, D. E. 1979 The high wave number instabilities of a Stokes wave. *J. Fluid Mech.* **93**, 491–500.

HATORI, M. 1984 Nonlinear properties of laboratory wind waves at energy containing frequencies. *J. Ocean. Soc. Japan* **40**, 1–18.

HATORI, M. & TOBA, Y. 1983 Transition of mechanically generated regular waves to wind waves under the action of wind. *J. Fluid Mech.* **130**, 397–409.

HATORI, M., TOKUDA, M. & TOBA, Y. 1981 Experimental study on strong interactions between regular waves and wind waves – I. *J. Ocean. Soc. Japan* **37**, 111–119.

HUANG, N. E. & LONG, S. R. 1980 An experimental study of the surface elevation probability distribution and statistics of wind generated waves. *J. Fluid Mech.* **101**, 179–200.

HUANG, N. E., BLIVEN, L. F., LONG, S. R. & DELEONIBUS, P. S. 1985 A study of the relationship among wind, wave and the drag coefficient. Submitted to *J. Geophys. Res.*

HUNT, J. N. 1952 Viscous damping of waves over an inclined bed in a channel of finite width. *Houille Blanche* **7**, 836–842.

IMAI, Y., HATORI, M., TOKUDA, M. & TOBA, Y. 1981 Experimental study on strong interaction between regular waves and wind waves – II. *Tohoku Geophys. J.* **28**, 87–103.

JACKSON, F. C. 1984 Some case studies of ocean wave physical processes utilizing the GSFC airborne radar ocean wave spectrometer. In *Remote Sensing of Oceans and Troposphere from Air and Space Platforms*, pp. 233–245. NASA Conference Pub. 2303.

LAKE, B. M. & YUEN, H. C. 1977 A note on some nonlinear water-wave experiments and the comparison of data with theory. *J. Fluid Mech.* **83**, 75–81.

LAKE, B. M. & YUEN, H. C. 1978 A new model for nonlinear wind waves. Part 1. Physical model and experimental evidence. *J. Fluid Mech.* **88**, 33–62.

LAKE, B. M., YUEN, H. C., RUNGLANDIER, H. & FERGUSON, W. E. 1977 Nonlinear deep-water waves: theory and experiment. Part 2. Evolution of a continuous wave train. *J. Fluid Mech.* **83**, 49–74.

LAMB, H. 1932 *Hydrodynamics*. Cambridge University Press.

LARSON, T. R. & WRIGHT, J. T. 1975 Wind-generated gravity–capillary waves: Laboratory measurements of temporal growth rates using microwave backscatter. *J. Fluid Mech.* **70**, 417–436.

LONGUET-HIGGINS, M. S. 1978 The instabilities of gravity waves of finite amplitude in deep water. *Proc. R. Soc. Lond.* A **360**, 471–505.

LONGUET-HIGGINS, M. S. 1980 Modulation of the amplitude of steep wind waves. *J. Fluid Mech.* **99**, 705–713.

MCLEAN, J. W. 1982*a* Instabilities of finite-amplitude water waves. *J. Fluid Mech.* **114**, 315–330.

MCLEAN, J. W. 1982*b* Instabilities of finite-amplitude gravity waves on water of finite depth. *J. Fluid Mech.* **114**, 331–341.

MCLEAN, J. W., MA, Y. C., MARTIN, D. U., SAFFMAN, P. G. & YUEN, H. C. 1981 Three-dimensional instability of finite amplitude water waves. *Phys. Rev. Lett.* **46**, 817–820.

MELVILLE, W. K. 1982 The instability and breaking of deep-water waves. *J. Fluid Mech.* **115**, 165–185.

MILES, J. W. 1967 Surface-wave damping in closed basins. *Proc. R. Soc. Lond.* A **297**, 459–475.

MITSUYASU, H. 1966 Interactions between water waves and wind (I). *Rep. Res. Inst. Appl. Mech., Kyushu University* **14**, 67–88.

MITSUYASU, H. & HONDA, T. 1982 Wind-induced growth of water waves. *J. Fluid Mech.* **123**, 425–442.

MOLLO-CHRISTENSEN, E. & RAMAMONJIARASOA, A. 1982 Subharmonic transition and group formation in a wind wave field. *J. Geophys. Res.* **87**, 5599–5717.

PHILLIPS, O. M. 1960 On the dynamics of unsteady gravity waves of finite amplitude. Part I. *J. Fluid Mech.* **9**, 193–217.

PHILLIPS, O. M. & BANNER, M. L. 1974 Wave breaking in the presence of wind drift and swell. *J. Fluid Mech.* **66**, 625–640.

PLANT, W. J. 1982 A relationship between wind stress and wave slope. *J. Geophys. Res.* **87**, 1961–1967.

REGIER, L. A. & DAVIS, R. E. 1977 Observations of the power and directional spectrum of ocean surface waves. *J. Mar. Res.* **35**, 433–452.

SHEMDIN, O. H. & HSU, E. Y. 1967 Direct measurement of aerodynamic pressure above a simple progressive gravity wave. *J. Fluid Mech.* **30**, 403–416.

SNYDER, R. L., DOBSON, F. W., ELLIOTT, J. A. & LONG, R. B. 1981 Array measurements of atmospheric pressure fluctuations above gravity waves. *J. Fluid Mech.* **102**, 1–59.

SU, M. Y., BERGIN, M., MARLER, P. & MYRICK, R. 1982 Experiments on nonlinear instabilities and evolution of steep gravity-wave trains. *J. Fluid Mech.* **124**, 45–72.

SU, M. Y. 1982 Three-dimensional deep-water waves. Part 1. Experimental measurements of skew and symmetric wave patterns. *J. Fluid Mech.* **124**, 73–108.

THOMPSON, T. W., WEISSMAN, D. E. & GONZALEZ, F. I. 1983 *L*-band radar back-scatter dependence upon surface wind stress: a summary of new SEASAT-1 and aircraft observations. *J. Geophys. Res.* **88**, 1727–1735.

TSIMRING, L. SH. 1983 Induced scattering of surface wind waves. *Izv. Acad. Nauk SSSR Atmos. and Ocean Phys.* **19**, 47–50.

WALSH, E. J., HANCOCK, D. W., HINES, D. E. & KENNEY, J. E. 1982 Development of the fetch-limited directional wave spectrum. In *Oceans '82 Conference Record*, pp. 820–825. Marine Tech. Soc., Wash., D.C.

WU, H. Y., HSU, E. Y. & STREET, R. L. 1977 The energy transfer due to air-input, non-linear wave–wave interactions and white cap dissipation associated with wind-generated waves. *Tech. Rep.* 207, pp. 1–158. Stanford Univ., Stanford, CA.

WU, H. Y., HSU, E. Y. & STREET, R. L. 1979 Experimental study of nonlinear wave–wave interaction and white-cap dissipation of wind-generated waves. *Dyn. Atmos. Oceans* **3**, 55–78.

ZAKHAROV, Y. E. 1968 Stability of periodic waves of finite amplitude on the surface of a deep fluid. *J. Appl. Mech. Tech. Phys.* **2**, 190–194.